JOURNAL OF GEOPHYSICAL RESEARCH, VOL. 113, B11405, doi:10.1029/2007JB005448, 2008

Body tides of a convecting, laterally heterogeneous, and aspherical Earth

Laurent Métivier[1] and Clinton P. Conrad[2]

Received 18 October 2007; revised 12 June 2008; accepted 30 July 2008; published 13 November 2008.

[1] Precise knowledge of Earth's body tides is crucial for correcting geodetic positioning measurements, satellite gravity surveys, and superconducting gravimeters with nanogal precision. With this aim, body tides are generally computed assuming a radially (or elliptically) stratified Earth. However, seismic tomography surveys and fluid dynamic studies show that thermal convection within Earth's mantle produces significant lateral heterogeneity exemplified by superplumes, superswells, and subducting slabs. To determine the influence of this heterogeneity on body tides, we used a tomographic model to constrain lateral variations in mantle density and rigidity. This heterogeneity drives convective flow that deflects Earth's surface and core-mantle boundaries by a few kilometers; we used a viscous flow model to constrain this dynamically supported asphericity. After verifying this complete Earth model using geoid observations, we used the spectral element method to determine how Earth's body tides are perturbed compared to a spherical Earth. We find maximum radial perturbations of surface and geoid displacements of 0.3 and 0.1 mm, respectively, and tidal gravity variations of 150 nGal. The amplitude of tidal gravity perturbations depends strongly on location and is greatest above large mantle density anomalies: e.g., large dense slabs (South America, Indonesia, Marianas), hot spots (Hawaii, Iceland), and the East African Rift. Predicted gravity perturbations are 100 times larger than the present precision of superconducting gravimeters and are comparable in magnitude to the unexplained residue observed at some gravimeter stations after tidal corrections. While this residue has been attributed to unmodeled loading from ocean tides, body tide perturbations caused by convection-induced mantle heterogeneity may contribute to this observed residue.

Citation: Métivier, L., and C. P. Conrad (2008), Body tides of a convecting, laterally heterogeneous, and aspherical Earth, *J. Geophys. Res.*, *113*, B11405, doi:10.1029/2007JB005448.

1. Introduction

[2] Every day, the gravitational attractions of the Moon and the Sun induce deformations of the solid Earth that produce time variations in surface deflections and gravity with amplitudes up to 50 cm and 200 μGal (1 μGal = 10^{-8} m s^{-2}), respectively. This body tide of the Earth exhibits periodicity on timescales between a few hours to a few tens of years and can be monitored today quite accurately using modern geodetic techniques, which have improved dramatically during the past three decades. Surface displacement can now be measured with a precision up to 1 mm using GPS or VLBI [e.g., *Petrov and Boy*, 2004] and gravity can be measured to a precision of 1 nGal (10^{-11} m s^{-2}) (in the tidal frequency band after integrating in time, see *Crossley et al.* [2001], *Rosat et al.* [2004], *Hinderer and Crossley* [2004], and *Van Camp et al.* [2005]) using superconducting gravimeters such as those used in observatory networks (see, for example, the GGP network [*Aldridge et al.*, 1991; *Hinderer and Crossley*, 2004]). Furthermore, time variations in the global gravity field are available from the GRACE mission (launched in 2002). These accurate geodetic data can be used to study a variety of geodynamic, hyrological, and atmospheric processes. However, to be useful, the time-varying solid Earth tide must be modeled so that its influence can be extracted from the observations. As instrument precision increases, the need for accurate models of the solid Earth body tides increases as well, which will be particularly important for the future GRACE Follow-On gravity satellite mission.

[3] Currently, tides are modeled using a classical model that assumes a layered ellipsoidal Earth (typically based on the PREM Earth model [*Dziewonski and Anderson*, 1981]), a hydrostatic state of equilibrium, and a fluid core [*Smith*, 1974; *Wahr*, 1981a, 1981b]. The effects of mantle anelasticity have also been included [*Wahr and Bergen*, 1986; *Dehant*, 1987]. However, Earth's internal structure is the result of a complex dynamical history and is well known to be more heterogeneous than in a Spherical Non Rotating Elastic Isotropic (SNREI) Earth model like PREM. In

[1]Department of Earth and Planetary Sciences, Johns Hopkins University, Baltimore, Maryland, USA.
[2]Department of Geology and Geophysics, University of Hawaii, Honolulu, Hawaii, USA.

0148-0227/08/2007JB005448$09.00

particular, it is widely accepted that the Earth's mantle is convecting in an effort to dissipate heat. This convection features dense slabs of subducted lithosphere that sink into the mantle beneath subduction zones [e.g., *van der Hilst et al.*, 1997], rising plumes that are several hundred kilometers wide [e.g., *Montelli et al.*, 2006] and possibly rising "superplumes" beneath Africa and the South Pacific that are several thousand kilometers wide [e.g., *Davaille*, 1999; *Romanowicz and Gung*, 2002; *Courtillot et al.*, 2003]. This dynamic mantle interior generates laterally varying heterogeneity that can be observed using seismic tomography [e.g., *Li and Romanowicz*, 1996; *Grand et al.*, 1997; *van der Hilst et al.*, 1997; *Ritsema et al.*, 1999; *Gu et al.*, 2001]. Such tomographic inversions constrain lateral and depth variations in compressional and/or shear wave speeds. Because these variations are generated by thermal convection and possibly chemical stratification [e.g., *Masters et al.*, 2000], tomographic images can place constraints on geodynamic models of mantle flow [e.g., *Becker and Boschi*, 2002]. Because seismic wave speeds depend on the density and elastic properties of rocks [e.g., *Dahlen and Tromp*, 1998], we can also use tomographic images to constrain lateral variations in the mantle's elastic parameters and densities. These lateral heterogeneities should perturb the Earth's body tides.

[4] Decades ago, a few authors presented a controversial correlation between unexplained tidal gravity measurements and heat flow surface anomalies [e.g., *Robinson*, 1989; *Melchior*, 1995]. As an explanation, they proposed that this correlation reflects the impact of lateral variations of crustal thickness on body tide deformations. However, considering the past precision of gravity measurements (more than 1 μGal), it is probably unlikely that the tidal impact of lateral heterogeneities could have been observed at that time [e.g., *Rydelek et al.*, 1991; *Métivier et al.*, 2007]. Today, with instrument precision one thousand times more accurate, the unexplained residue that can be observed in superconducting gravimeter measurements is generally considered to be caused by loading induced by oceanic tides, which are not sufficiently well modeled. For gravity measurements, this residue has amplitudes as large as 200–300 nGal in the tidal frequency band [*Agnew*, 1995; *Boy et al.*, 2003; *Baker and Bos*, 2003; *Bos and Baker*, 2005]. However, the possibility remains that some of this unexplained residue may be caused by unmodeled aspects of the body tides, such as those caused by the mantle's laterally heterogeneous structure.

[5] A few studies have investigated the effects of the internally heterogeneous structure of the Earth on body tide deformations. *Molodenskiy* [1977] was the first to address this problem. He investigated a variational approach of the elastogravitational equations and their first-order perturbations induced by lateral variations and topographies. Following this approach, *Wang* [1991] computed a viscoelatic model of the Earth body tides with low-degree theoretical lateral variations of density and of rheological parameters. Then *Dehant et al.* [1999] studied the influence of the nonhydrostatic ellipticity of internal boundaries on body tides. These different studies showed that the effect of low-degree lateral variations on body tides is small but not necessarily negligible compared to present accuracy of gravimeter data. Yet these studies did not take into account the entire complexity of mantle structure and asphericity of the Earth. *Wang* [1991] assumed an aspherical Earth model with very long wavelength lateral heterogeneities (up to degree 8) and no dynamic topography, whereas *Dehant et al.* [1999] assumed an Earth model with elliptic dynamic topography but without internal lateral heterogeneities. Recently, *Métivier et al.* [2005, 2006] developed a new model of elastogravitational deformations based on a spectral element method [e.g., *Komatitsch and Tromp*, 1999; *Chaljub et al.*, 2003]. This model can take into account lateral variations of density and elastic parameters within the mantle and the crust, as well as variations in topography on the surface or on internal interfaces (the core-mantle boundary (CMB), for example), and the nonhydrostatic state of prestress of the planet. *Métivier et al.* [2007] presented a first application of this model investigating the possible impact of two large density anomalies associated with superplumes beneath Africa and the South Pacific, as well as the dynamic topography associated with the mass anomalies. They showed that such heterogeneities could induce perturbations on surface tidal gravity that are more than 100 times larger than present precision of superconducting gravimeters, which is at the level of presently observed measurement residue. Moreover, they also showed that only large mantle-scale heterogeneities would be able to significantly perturb body tide deformations and tidal gravity variations.

[6] More recently, *Fu and Sun* [2007] investigated the impact of lateral heterogeneity on body tides using density and elasticity constraints from a seismic tomography model. However, this study did not fully consider the mantle convection processes that generated the heterogeneity observed by tomography. For example, this study did not account for the nonhydrostatic state of prestress within the mantle, although *Métivier et al.* [2007] suggested that this effect can probably be neglected. More importantly, however, they did not address the fact that density anomalies in the mantle are dynamically supported by vertical deflections of the surface and the CMB. It is well known that, by itself, the density distribution of the mantle inferred from tomography cannot explain Earth's geoid anomalies [*Hager*, 1984; *Richards and Hager*, 1984]. Instead, the dynamics of a viscous mantle must be considered, in which dynamic mantle flow deflects both the surface and the core-mantle boundary to create dynamically supported topography on these interfaces. This dynamic topography can be predicted using viscous flow models [e.g., *Hager*, 1984; *Gurnis*, 1993] and is required to explain the Earth's geoid [e.g., *Hager*, 1984; *Richards and Hager*, 1984; *Thoraval and Richards*, 1997; *Čadek and Fleitout*, 2003]. Models generally predict amplitudes of 1–2 km of surface topography, which have been correlated with long-wavelength topographic features around the world such as southern African plateaus [e.g., *Lithgow-Bertelloni and Silver* 1998], topographic asymmetry across the North Atlantic [*Conrad et al.*, 2004], and anomalously deep back-arc basins [*Husson*, 2006]. Geologically constrained uplift and subsidence events have also been attributed to time-varying dynamic topography [e.g., *Mitrovica et al.*, 1989; *Pysklywec and Mitrovica*, 1998; *Conrad and Gurnis*, 2003]. Most importantly for the prediction of body tides, the density heterogeneity associated with this "dynamic topography" is of a

magnitude comparable to that of the internal heterogeneity itself [e.g., *Hager* 1984]. Therefore, a proper treatment of the effect of mantle convection on the Earth's body tides should include both the mantle's internal heterogeneity and the dynamic topography produced by this heterogeneity within a viscous mantle.

[7] In this study, we used a tomographic model of mantle shear velocity to determine mantle density and rigidity parameter distributions within the Earth. We then calculate viscous mantle flow driven by this density heterogeneity model and determine the dynamic topography that is created by this flow on the surface and the CMB. Using this new physical model of the solid Earth, we investigate tidal deformation and gravity time variations of the planet. We investigate the various primary components of tides (semi-diurnal, diurnal, and longer-period components) and constrain which aspects of mantle convection are most important for perturbing these body tides.

2. Viscous Flow in the Earth's Mantle

[8] Mantle flow supports a few kilometers of dynamic topography on Earth's surface and internal boundaries. Although this dynamic topography cannot be detected directly from global seismic tomography observations, which typically have 100 km radial resolution, it induces lateral variations thought to be particularly important on the CMB and the surface (due to the large density contrasts there) and cannot be neglected in a 3D Earth model. In general, dynamically supported topography is difficult to constrain directly because isostatically supported crustal thickness variations obscure dynamic topography and make its detection difficult [*Colin and Fleitout*, 1990].

[9] To constrain this dynamic topography, which must accompany internal heterogeneity inferred from tomographic studies, we employ a spherical finite element code (CitComS [*Moresi et al.*, 1996; *Zhong et al.*, 2000]) to predict instantaneous mantle flow driven by the mantle's internal density heterogeneity. We used the tomography model S20RTSb [*Ritsema et al.*, 2004] to infer lateral variations of density within the mantle (see Figure 1, bottom) and use a constant velocity-density conversion factor of 0.15 g cm^{-3} km^{-1} s to convert seismic velocity anomaly to density anomaly. We chose this conversion factor because it is consistent with both laboratory data [e.g., *Karato and Karki* 2001] and with previous studies [e.g., *Behn et al.*, 2004; *Conrad et al.*, 2007]. Also following previous work [e.g., *Lithgow-Bertelloni and Richards*, 1998; *Behn et al.*, 2004], we do not impose density anomalies above 300 km depth because seismically fast velocity anomalies associated with continental roots have been shown to correspond to neutrally buoyant ''tectosphere'' [e.g., *Jordan*, 1975], which implies that a straightforward conversion between seismic velocity and density is not appropriate for the continental lithosphere. We employ free slip boundary conditions at the surface and CMB, and assume a radially symmetric viscosity structure for the mantle that is consistent with the one used by *Lithgow-Bertelloni and Richards* [1998] to successfully reproduce the observed geoid. The resulting mantle flow (Figure 1) shows upwellings and downwellings associated with low and high mantle density anomalies. Finally, lateral variations in rigidity are also inferred from the tomography model using the classical relation linking shear velocity, density and rigidity ($V_s = \sqrt{\mu/\rho}$, assuming an isotropic media) [*Dahlen and Tromp*, 1998].

[10] Dynamic topography is calculated by converting radial tractions, σ_{zz}, on the undeformable surface and CMB interfaces of these calculations into the topography, h, that would form on a free surface using the relationship $\sigma_{zz} = \Delta\rho g h$, where $\Delta\rho$ is the density contrast across the interface and g is the acceleration due to gravity [e.g., *Lithgow-Bertelloni and Silver*, 1998; *Conrad et al.*, 2004]. To do this, we assumed $\Delta\rho = 2300$ kg m^{-3} for oceans (as has been used by others [*Conrad et al.*, 2004], corresponding to the density difference between mantle rocks and water, the oceanic crust being neglected because of its small mean thickness) and $\Delta\rho = 2800$ kg m^{-3} for continents (the density difference between crustal rocks and air). For the CMB, we assumed $\Delta\rho = 4336$ kg m^{-3} and $g = 10.688$ m s^{-2}. Applying this calculation to the above described flow models (Figure 1, top) shows that Earth's surface presents positive dynamic topography over the two ''superplumes'' beneath southern Africa and the southern Pacific [*Davaille*, 1999], and negative dynamic topography near the major subduction zones of South America and Southeast Asia. The predicted spatial patterns, as well as the predicted peak amplitudes of nearly 2 km, are consistent with previous models of dynamic topography that have been constrained using geologic observations [e.g., *Lithgow-Bertelloni and Silver*, 1998; *Conrad et al.*, 2004]. Models that drive flow using only density heterogeneity in the upper or lower mantles show that these two regions contribute approximately equally to the net surface dynamic topography (Figure 2), each generating up to 1 km of dynamic topography at the surface.

[11] To demonstrate the importance of dynamic topography to the Earth's lateral density heterogeneity structure, we calculated the geoid topography of our laterally heterogeneous Earth model both with (Figure 3b) and without (Figure 3a) a contribution from dynamic topography. To do this, we solved the Poisson equation using a spectral element code based on the *Métivier et al.* [2006] method. The geoid predicted without dynamic topography (Figure 3a) exhibits amplitudes that are more than 4 times larger than the observations (Figure 3c), as well as a very different spatial pattern. Both the amplitudes and the spatial pattern are dramatically improved for the geoid prediction that includes dynamic topography (Figure 3b). The importance of dynamic topography for reproducing the global geoid signal has been known for some time [e.g., *Hager*, 1984; *Richards and Hager*, 1984; *Thoraval and Richards*, 1997; *Čadek and Fleitout*, 2003]; we demonstrate this importance here to emphasize the need to treat both internal density heterogeneity and dynamic topography when evaluating the effect of lateral heterogeneity on body tide deformations. The positive comparison between predicted (Figure 3b) and observed (Figure 3c) geoids also serves to validate our model for the mantle's internal density heterogeneity. Some of the differences between (Figure 3b) and (Figure 3c) may be associated with unmodeled deep Earth structure or flow but are probably dominated by our exclusion of density anomalies shallower than 300 km, as well as surface tectonic features such as subduction or

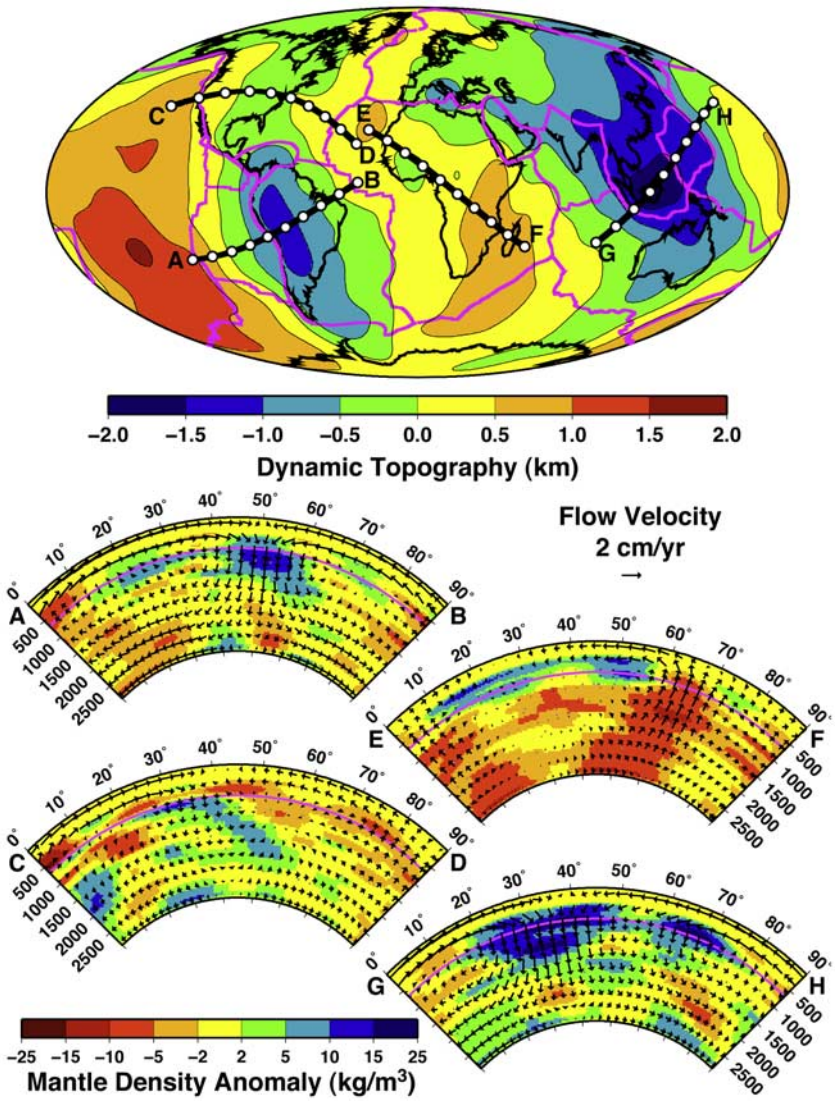

Figure 1. (top) Predicted dynamic topography on the Earth's surface and (bottom) cross sections, calculated assuming a laterally varying mantle density heterogeneity (colors in cross sections) that drives a model of mantle flow (arrows in cross sections).

lithospheric deformations that can contribute to the geoid shape. However, for the present work, these density anomalies are probably too "superficial" to significantly perturb body tide deformations [see *Métivier et al.*, 2007].

3. Body Tide Modeling

[12] In this work we used a new body tide model, developed by *Métivier et al.* [2005, 2006], which is dedicated to the calculation of elastogravitational deformation assuming a laterally varying Earth structure. This model is based on perturbation theory [e.g., *Woodhouse and Dahlen*, 1978; *Dahlen and Tromp*, 1998], and the equations are solved using the spectral element method [e.g., *Komatitsch and Tromp*, 1999; *Chaljub et al.*, 2003]. The main advantages of this method are that (1) grid discretization methods are better adapted than spherical harmonic expansions for investigating both global and local deformation problems of heterogeneous and aspherical planets and (2) the numerical method is easily parallelized and thus can utilize modern parallel-computing facilities. The present model has been coded in Fortran 90 using a structural formalism, and runs in parallel using message passing interface (MPI).

[13] The model has been successfully validated for several well-known related problems [*Métivier et al.*, 2005; *Greff-Lefftz et al.*, 2005; *Métivier et al.*, 2006] involving the Earth's hydostatic ellipticity, and was first applied by *Métivier et al.* [2007]. Here we use an updated version of this model. In a laterally heterogeneous Earth, couplings between the harmonic components of the tidal potential (primarily a degree 2 signal) and the harmonic components of the heterogeneity distribution (from degree 1 to 20) also induce tidal deformations of degrees 0 and 1, which are singular components [*Métivier et al.*, 2006]. New validation tests have been made in order to strengthen the treatment of these degree 0 and degree 1 components of the tidal deformation solution. They are

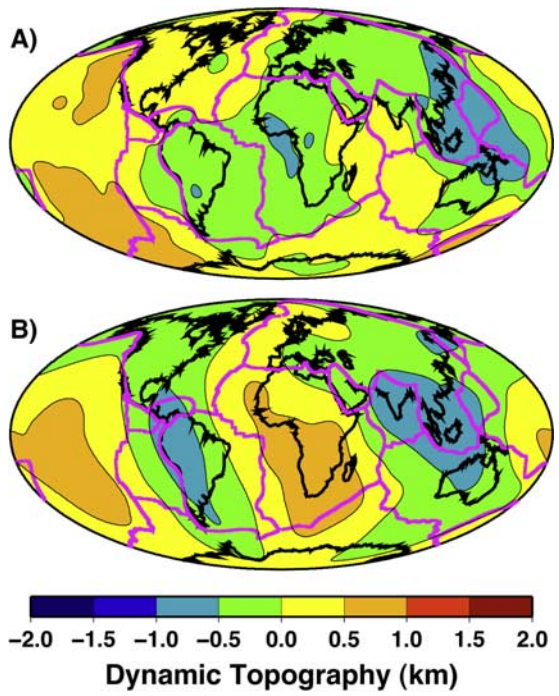

Figure 2. Dynamic topography on the Earth's surface calculated assuming (a) only lateral variations of density in the upper mantle and (b) only lateral variations of density in the lower mantle. The sum of Figures 2a and 2b produces the net dynamic topography shown in Figure 1.

now solved separately, which globally improves the precision of degree 0 and degree 1 solutions, as well as the precision of the other degree components. In addition, in this work, we neglected the nonhydrostatic component of prestress induced by the mantle convection. *Métivier et al.* [2007] showed that its impact on body tides is very small compared to the effect of lateral variations in density and elastic parameters, and of dynamic topography.

4. Impact of Mantle Dynamics on Body Tides

[14] Body tide deformations of terrestrial planets are usually calculated assuming a planet with a spherical symmetry and a hydrostatic state of equilibrium. It is well known since the work of *Love* [1911] that for spherically symmetric models, surface displacements and surface gravity variations can be expressed in terms of dimensionless coefficients known as Love numbers, which depend only on the spherical harmonic degree. Here we calculate perturbations to the classical Love numbers that are caused by the nonsphericity and nonsymmetry of the Earth associated with thermal convection. As we shall see, the resulting tidal perturbations have large amplitudes near regions where thermal convection produces significant mantle heterogeneity.

4.1. Perturbation of Love Numbers

[15] Let us denote V as the tide-generating potential exerted on the Earth (defined here such that the tidal gravitational attraction is equal to $+\nabla V$), mostly induced by the attractions of the Moon and the Sun. V is classically expanded using spherical harmonics, as follows:

$$V(r,\theta,\varphi,t) = \sum_{n=2}^{\infty} \sum_{m=-n}^{n} \left(\frac{r}{a}\right)^n V_{nm}(t)\ Y_{nm}(\theta,\varphi), \qquad (1)$$

where r, θ, and φ are the spherical coordinates, a is the Earth's mean radius, V_{nm} is the spherical harmonic coefficient, and Y_{nm} is the spherical harmonic function of

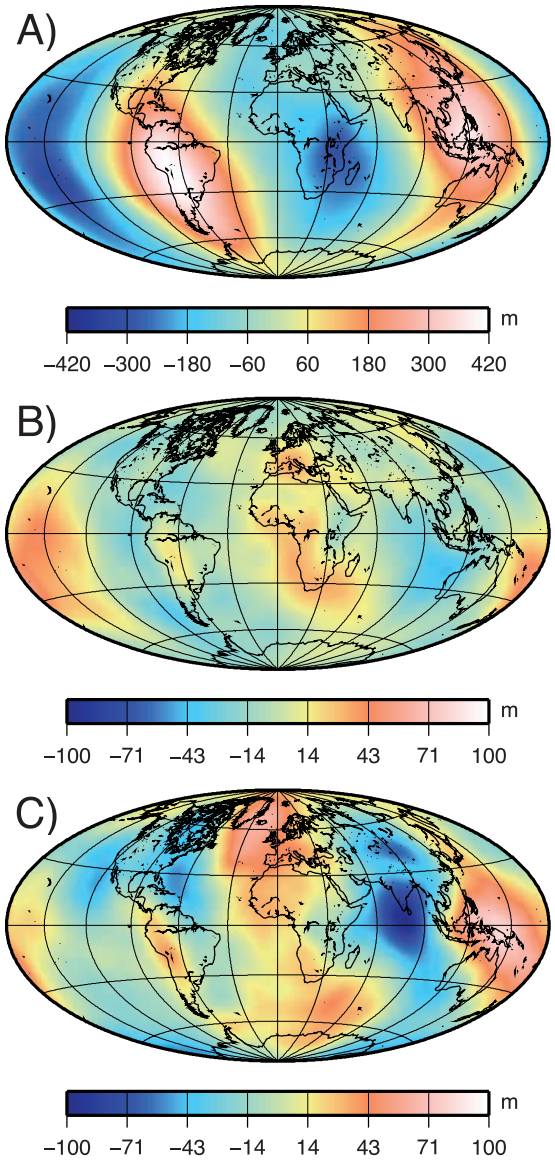

Figure 3. (a) The geoid topography of a spherical Earth with mantle density anomalies inferred from the tomographic model alone. (b) The geoid topography of an Earth model presenting the same internal mantle structure as in Figure 3a, as well as the dynamic topographies on surface and CMB (see Figure 1). (c) The observed geoid determined from the GRACE mission (up to degree 20) [*Tapley et al.*, 2005; *Reigber et al.*, 2005].

degree n and order m. In this work we use the following spherical harmonic definition:

$$Y_{nm}(\theta,\varphi)=\sqrt{(2n+1)\frac{(n-|m|)!}{(n+|m|)!}(2-\delta_{0m})}\cdot P_{n|m|}(\cos\theta)\begin{cases}\cos(m\varphi) & \text{if } m\le 0\\ \sin(m\varphi) & \text{if } m>0,\end{cases} \tag{2}$$

where P_{nm} is the associated Legendre function of degree n and order m. V_{nm} coefficients depend mostly on the orbit of the Moon and the Sun and can be calculated precisely using ephemeris (see, e.g., the catalogue of *Hartmann and Wenzel* [1995]). The luni-solar tide-generating potential is mostly of degree 2 and can be divided into three main types of wave tides: semidiurnal tides for $|m| = 2$ (e.g., M_2, S_2, N_2 tidal harmonics), diurnal tides for $|m| = 1$ (e.g., O_1, P_1, K_1 tidal harmonics) and long-period tides for $m = 0$ (e.g., S_a, S_{sa} tidal harmonics). In this work we will only focus on these three types, which together represent in power approximately 99.98% of the total tide-generating potential power (calculation based on the work by *Hartmann and Wenzel* [1995]).

[16] Let us define $\mathbf{u}$ as the Earth's surface displacement induced by the tide-generating potential and ϕ as the surface gravitational potential created by internal mass redistributions. Then $\phi + V(r = a)$ is the total tidal gravitational potential on the Earth's surface (for the exterior of the solid Earth, i.e., the free space potential). Finally, we denote g as the magnitude of tidal gravity, which could be measured on the Earth's moving surface. Love numbers h_n, l_n, and k_n (l_n is also called the Shida number) and the delta number δ_n are defined such as

$$\mathbf{u}(\theta,\varphi)=\sum_{n=0}^{\infty}\sum_{m=-n}^{n}\frac{V_{nm}}{g_o}(h_nY_{nm}(\theta,\varphi)\ \mathbf{e}_r+\ l_n\ \nabla_1 Y_{nm}(\theta,\varphi)), \tag{3}$$

$$\phi(\theta,\varphi)+V(a,\theta,\varphi)=\sum_{n=0}^{\infty}\sum_{m=-n}^{n}V_{nm}\ (1+k_n)Y_{nm}(\theta,\varphi), \tag{4}$$

$$g(\theta,\varphi)=-\sum_{n=0}^{\infty}\sum_{m=-n}^{n}\frac{n}{a}\ V_{nm}\ \delta_nY_{nm}(\theta,\varphi), \tag{5}$$

where g_o is the mean surface gravity, $\mathbf{e}_r$ is the radial unit vector ($\mathbf{e}_\theta$ and $\mathbf{e}_\varphi$ are colatitude and longitude unit vectors, respectively), and ∇_1 is the surface unit gradient ($\nabla_1 = \mathbf{e}_\theta\partial_\theta + \mathbf{e}_\varphi \sin\theta^{-1}\partial_\varphi$). In this study we only focus on degree 2 tidal deformations. For the PREM Earth model, the degree 2 Love and delta numbers are approximately

$$h_2=0.603741,\quad l_2=0.084010,\quad k_2=0.298231,\quad \delta_2=1.156394. \tag{6}$$

These values are valid for a quasi-static approximation (the inertial term is neglected). Technically, Love numbers depend also slightly on frequency, rotation and anelasticity, but these aspects of radially symmetric Earth models are beyond the scope of this study (for more information about classical determinations of Love numbers, see [*Wahr* [1981b], *Wahr and Bergen* [1986], *Dehant* [1987], and *Mathews et al.* [1995]). Note that the negative sign for g is due to the fact that g is the magnitude and not the radially oriented component of the tidal gravity. We focus here on magnitude determination of gravity because this is the quantity that is measured by gravimeters.

[17] Let us now assume a more complex Earth model that is not spherical and presents lateral heterogeneities of density or elastic parameters within the mantle. We denote $\delta\mathbf{u}$ as the perturbation to the tidal surface displacement that is induced by the difference between the total Earth model and the radially symmetric Earth model (PREM in our case). We similarly define $\delta\phi$ as the perturbation of surface tidal free space potential, and δg as the perturbation of surface tidal gravity on the Earth's moving surface. Note that if $\mathbf{u}$ is expressed on the spherical PREM surface, $\mathbf{u} + \delta\mathbf{u}$ corresponds to the total tidal displacement expressed on the aspherical Earth model surface. Expressed differently, $\phi + V + \delta\phi$ is the total free space potential, which is traditionally expressed on the mean spherical surface of the Earth (PREM Earth's surface here). Finally, g is the gravity variation on the PREM surface deformed by $\mathbf{u}$, whereas $g + \delta g$ is the gravity variation on the aspherical Earth model surface deformed by $\mathbf{u} + \delta\mathbf{u}$. The calculations of $\delta\mathbf{u}$, $\delta\phi$, and δg are detailed by *Greff-Lefftz et al.* [2005] and *Métivier et al.* [2006].

[18] One can express all of these perturbation functions using Love number formalism and spherical harmonic expansion. However, the bias from the radially symmetric model induces infinite couplings between spherical harmonics, which means that a Love number at a given degree would have an infinite number of small perturbations (one for each spherical harmonics degree and order). We can define tidal displacement, potential and gravity on every surface angular position (θ, φ) as follows:

$$\begin{aligned}\mathbf{u}+\delta\mathbf{u}=\sum_{m=-2}^{2}\frac{V_{2m}}{g_o}\Big[\Big(&h_2Y_{2m}(\theta,\varphi)\ \mathbf{e}_r+\ l_2\ \nabla_1Y_{2m}(\theta,\varphi)).\\ &+\sum_{n'=0}^{\infty}\sum_{m'=-n'}^{n'}\Big(\delta h_{2m}^{n'm'}Y_{n'm'}(\theta,\varphi)\ \mathbf{e}_r+\delta l_{2m}^{n'm'}\ \nabla_1Y_{n'm'}(\theta,\varphi)\\ &-\delta w_{2m}^{n'm'}\ \mathbf{e}_r\wedge\nabla_1Y_{n'm'}(\theta,\varphi)\Big)\Big],\end{aligned} \tag{7}$$

$$\begin{aligned}\phi+V+\delta\phi=\sum_{m=-2}^{2}V_{2m}\Big[&(1+k_2)Y_{2m}(\theta,\varphi)\\ &+\sum_{n'=0}^{+\infty}\sum_{m'=-n'}^{+n'}\delta k_{2m}^{n'm'}Y_{n'm'}(\theta,\varphi)\Big],\end{aligned} \tag{8}$$

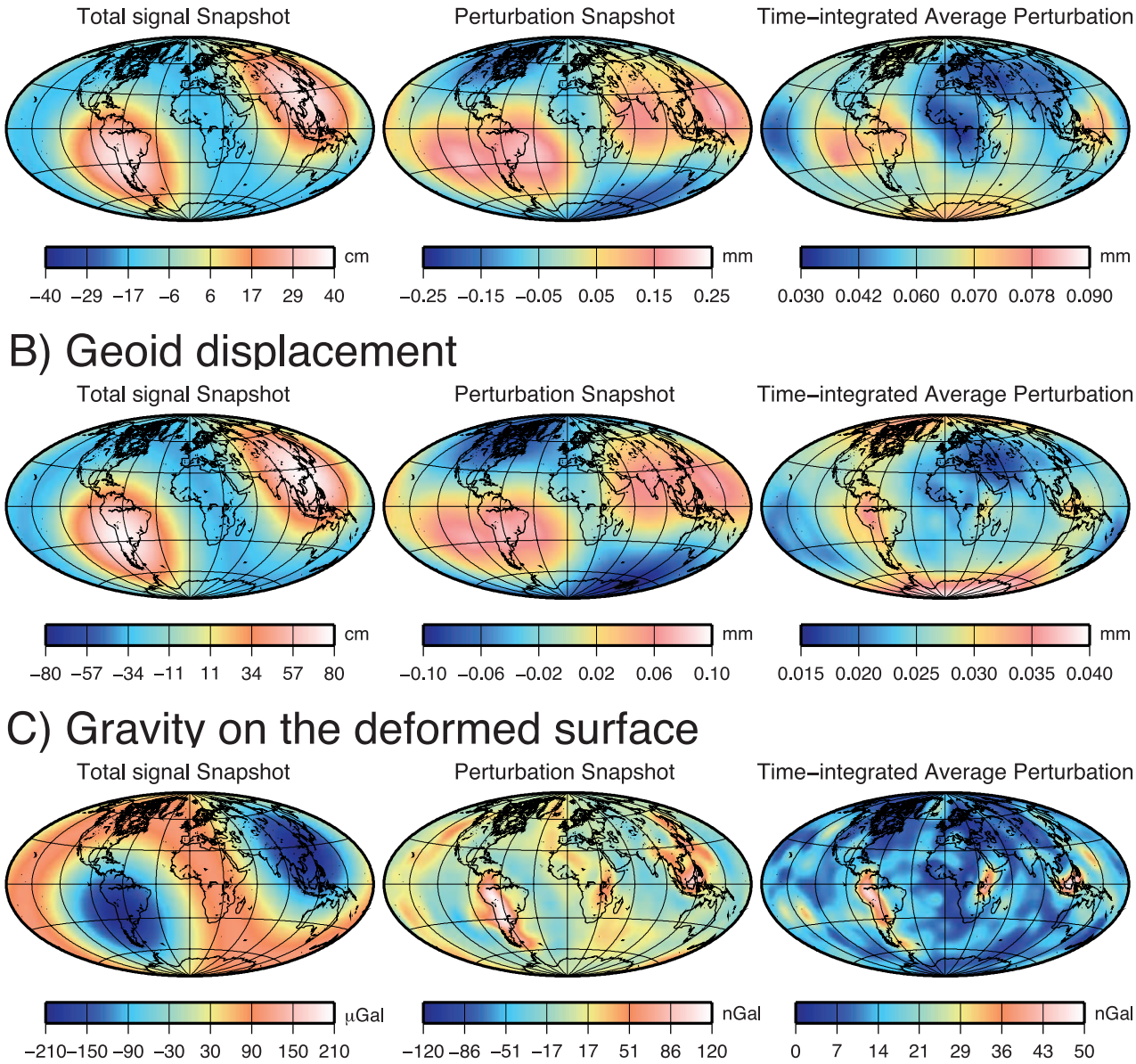

Figure 4. (a) Surface displacements, (b) geoid displacements, and (c) gravity variations induced by the tide-generating potential on a given date or integrated over time. (left) Maps of the tidal responses for the PREM Earth model, on 23 November 2007 at 1800 UTC. (middle) Maps of additional tidal perturbations that are due to lateral heterogeneities in the mantle and to topographies on the surface and on the CMB, on the same date. (right) Maps of the mean integration of the perturbations over 1 year (see equation (10)).

$$g + \delta g = -\sum_{m=-2}^{2} \frac{2}{a} V_{2m} \left[\delta_2 Y_{2m}(\theta, \varphi) + \sum_{n'=0}^{+\infty} \sum_{m'=-n'}^{+n'} \delta\delta_{2m}^{n'm'} Y_{n'm'}(\theta, \varphi) \right], \quad (9)$$

where $\delta h_{nm}^{n'm'}$, $\delta l_{nm}^{n'm'}$, $\delta k_{nm}^{n'm'}$ and $\delta\delta_{nm}^{n'm'}$ are degree n' and order m' perturbations of the degree n and order m Love and delta numbers. Asphericity and heterogeneities also produce toroidal tidal deformations that do not exist in a radially symmetric Earth model. The toroidal Love number perturbation is denoted by $\delta w_{nm}^{n'm'}$.

[19] We calculated the Earth's tidal response using the numerical code of *Métivier et al.* [2006]. The Love number perturbations have been inferred from the numerical solution for our laterally heterogeneous and aspherical Earth using discrete Legendre transforms up to degree 20, and are given in Tables S1–S3 in the auxiliary material.[1] Knowing

[1] Auxiliary materials are available in the HTML. doi:10.1029/2007JB005448.

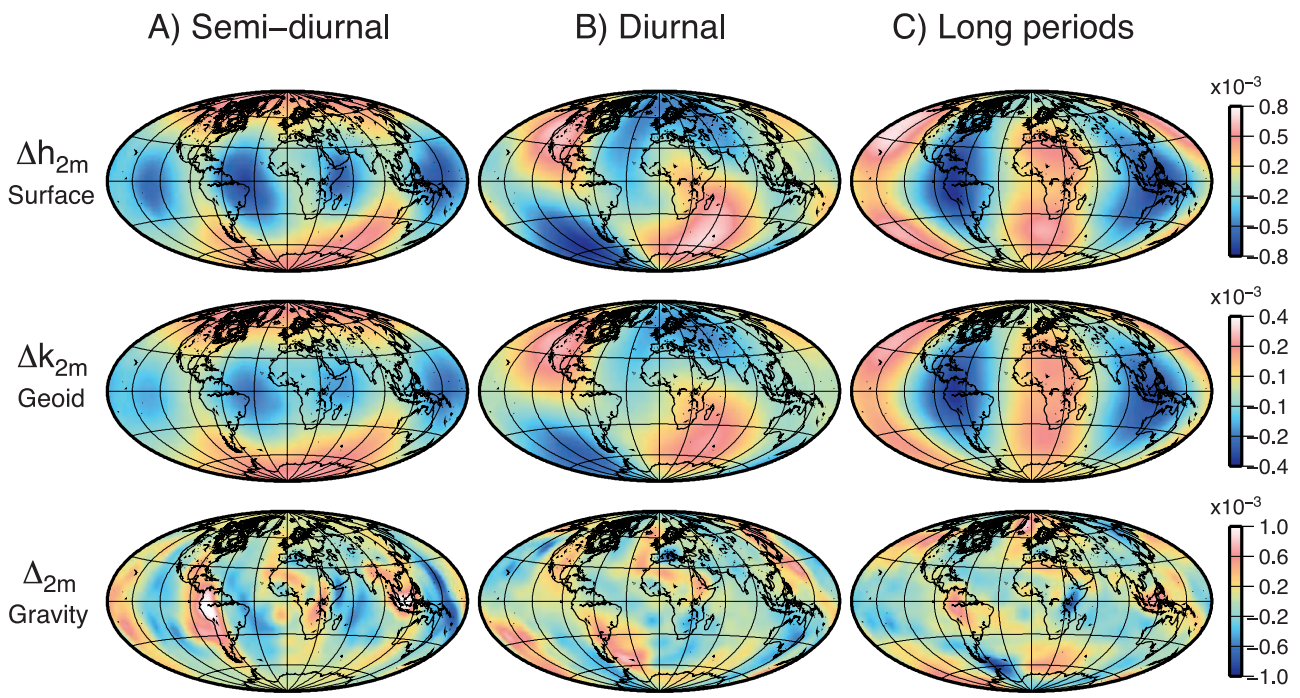

Figure 5. Maps of (top) the harmonic components of the surface displacement perturbations, (middle) the geoid displacement perturbations, and (bottom) the tidal gravity perturbations, i.e., Δh_{2m}, Δk_{2m}, and Δ_{2m}, respectively, quantities (see equations (12)–(16)), with (a) $m = -2$ for the semidiurnal component, (b) $m = -1$ for the diurnal component, and (c) $m = 0$ for the long-period component.

these numbers and their tide-generating potential coefficients, one can calculate tidal perturbations due to mantle convection everywhere on the Earth at any given time. As an example, we have calculated the surface displacement (Figure 4a), geoid displacement (Figure 4b) and gravity variation (Figure 4c) induced by the tide-generating potential on 23 November 2007 at 1800 UTC (maps on the left side and on the middle). We chose this date because its tide-generating potential is quite large (it is close to winter solstice when diurnal tides are maximum), and because the pattern of tidal perturbations is typical and shows interesting features. To illuminate the influence of lateral heterogeneity, we show maps of the total signal of the three fields (Figure 4, left) and of the additional tidal perturbations that are due to lateral heterogeneities in the mantle and to dynamic topography on the surface and on the CMB (Figure 4, middle). Finally, in order to confirm the relevance of these snapshots, we also integrate the different fields over a given time period. Maps on Figure 4 (right) present the mean values of these time integrations over 1 year (from 23 November 2007 to 23 November 2008), calculated as follows:

$$f_{mean}(\theta,\phi) = \sqrt{\frac{1}{T}\int_0^T f(\theta,\phi)^2 dt}, \qquad (10)$$

where f is the given field being investigated and $T = 365$ days. To construct each map, we summed 8640 other maps, one every hour.

[20] Surface and geoid displacement perturbations are less than 0.5 mm and occur over long wavelengths of harmonic degree three and higher (Figures 4a and 4b) and are even smaller for the time-integrated mean. Given the sensitivity of modern geodesy, it would be difficult today to measure such perturbations. For gravity, however, we see that the effect of mantle heterogeneities on body tides is of order 1‰, and the perturbations exhibit a very different spatial pattern with shorter wavelengths than the total amplitudes (Figures 4c). These shorter wavelengths arise because perturbations are more sensitive than the geoid to shallow heterogeneities. For gravity, perturbations up to 120 nGal are possible, which greatly exceeds superconducting gravimeter precision, and is almost at the level of noise that supposedly arises from unmodeled oceanic tidal loading [*Agnew*, 1995; *Boy et al.*, 2003; *Baker and Bos*, 2003; *Bos and Baker*, 2005]. Perturbation amplitudes of 120 nGal, however, only occur for specific regions that are geodynamically active, only some of which are obvious for the time shown in the snapshot of Figure 4c. In particular, large amplitudes (Figure 4c, right) are associated with major subduction zones along the west coast of South America as well as near east Asia (particularly in Indonesia and along Marianas subduction zone). Although less clear for the time shown in Figure 4c, large amplitudes are also associated with low-velocity seismic anomalies (superplumes) of eastern Africa and the central Pacific. The time-integrated map of gravity confirms that the largest tidal gravity perturbations occur in South America, East Africa, and Indonesia. In addition, we confirm that the pattern observed in the Figure 4 snapshot for gravity is typical.

[21] Finally, smaller amplitude perturbations can be seen above a few well known hot spots like Hawaii and Iceland, and even over the Mediterranean subduction zones close to

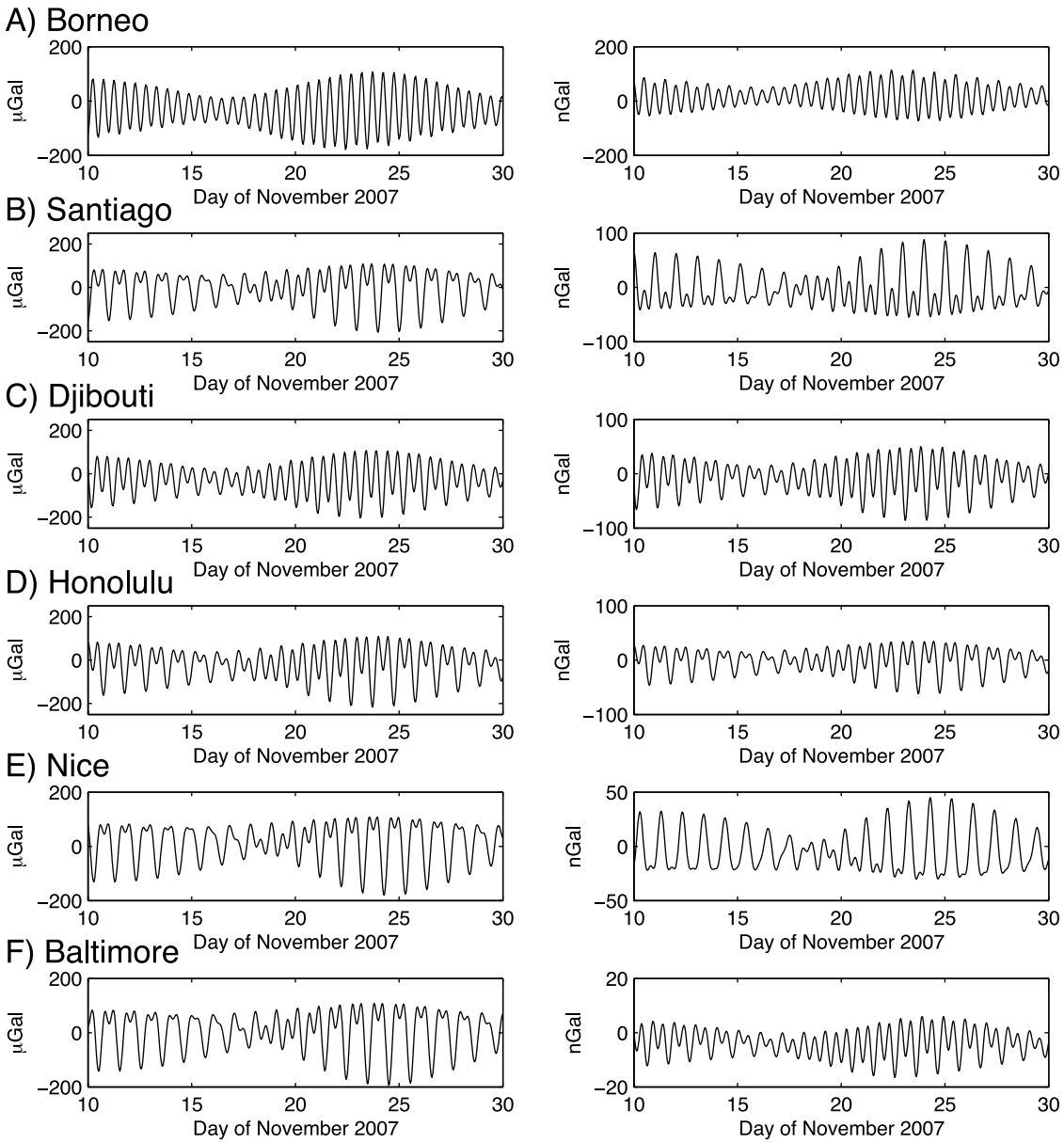

Figure 6. Prediction of tidal gravity variations in (a) Borneo (2°S, 111°E), Indonesia, (b) Santiago (33.5°S, 289.4°E), Chile, (c) Djibouti (11.6°N, 43.1°E), Djibouti, (d) Honolulu (19.6°N, 204.5°E), Hawaii, (e) Nice (43.7°N, 7.27°E), France, and (f) Baltimore (39.3°N, 283.4°E), Maryland, during November 2007. (left) Graphs showing the tidal signal calculated for the PREM Earth model. (right) Graphs of additional perturbations due to mantle lateral heterogeneities and to surface and CMB topographies.

Italy and southeastern France. These smaller features are also evident in the semidiurnal (Figure 5a), diurnal (Figure 5b), and long-period (Figure 5c) harmonics of gravity, geoid, and surface displacement perturbations. We denote Δ_{2m}, Δk_{2m} and Δh_{2m} as the geographical distributions of these harmonics. On the basis of equations (7)–(9), we have

$$\delta g(\theta,\phi,t) = -\sum_{m=-2}^{2} \frac{2}{a}\, V_{2m}(t) \left[\sum_{n'=0}^{+\infty} \sum_{m'=-n'}^{+n'} \delta\delta_{2m}^{n'm'}\, Y_{n'm'}(\theta,\varphi)\right], \tag{11}$$

$$\delta g(\theta,\phi,t) = -\sum_{m=-2}^{2} \frac{2}{a}\, V_{2m}(t)\, \Delta_{2m}(\theta,\phi) \tag{12}$$

$$\delta u_r(\theta,\phi,t) = \sum_{m=-2}^{2} \frac{V_{2m}(t)}{g_o} \left[\sum_{n'=0}^{\infty} \sum_{m'=-n'}^{n'} \delta h_{2m}^{n'm'}\, Y_{n'm'}(\theta,\varphi)\right], \tag{13}$$

Table 1. Relative Effect of Mantle Dynamics on Tidal Gravity at Various Locations With Respect to the Tidal Gravity of the PREM Earth Model[a]

			Diurnal		Semidiurnal	
	Maximum Ratio (November 2007)	Long Periods $m = 0$	$m = -1$	$m = 1$	$m = -2$	$m = 2$
Borneo	0.065%	−0.056%	-	-	−0.062%	−0.063%
Santiago	0.043%	-	−0.036%	−0.044%	−0.051%	−0.035%
Djibouti	0.042%	0.028%	0.044%	0.068%	-	0.036%
Honolulu	0.029%	0.016%	0.032%	0.033%	0.028%	0.031%
Nice	0.025%	−0.033%	−0.028%	−0.014%	−0.020%	−0.002%
Baltimore	0.009%	-	−0.006%	−0.003%	−0.004%	−0.022%

[a]The maximum ratio presents the ratio between the maximum absolute tidal gravity perturbation and the maximum absolute tidal gravity of PREM in November 2007 (see Figures 6 and 7). The relative perturbation for the different harmonics of the signal (Δ_{2m}), which are independent of time, are given. A blank entry means that the harmonic component of the tidal potential is close to zero at this location and thus the ratio has no geophysical meaning.

$$\delta u_r(\theta,\phi,t) = \sum_{m=-2}^{2} \frac{V_{2m}(t)}{g_o}\ \Delta h_{2m}(\theta,\phi), \tag{14}$$

$$\delta\phi(\theta,\phi,t) = \sum_{m=-2}^{2} V_{2m}(t)\left[\sum_{n'=0}^{+\infty}\sum_{m'=-n'}^{+n'} \delta k_{2m}^{n'm'} Y_{n'm'}(\theta,\varphi)\right], \tag{15}$$

$$\delta\phi(\theta,\phi,t) = \sum_{m=-2}^{2} V_{2m}(t)\ \Delta k_{2m}(\theta,\phi). \tag{16}$$

Figure 5 presents Δ_{2m}, Δh_{2m} and Δk_{2m}, which are independent of time, for $m = -2$, $m = -1$ and $m = 0$, which are the semidiurnal, the diurnal and the long-period cosinus components of the tidal perturbation, respectively. Anomalies in southern Europe are more clearly visible on the Δ_{2m} diurnal map. Large anomalies can also be seen on the diurnal and long-period maps over the South Sandwich trench and on the Scotia plate. Using this harmonic formalism, one can compare our results with results obtained by *Wang* [1991], who investigated the effect of mantle heterogeneities, up to degree 8, on the M2 body tide response of the Earth. Despite the fact that *Wang* [1991] did not take into account dynamic topography, we found close agreement between our results and *Wang*'s [1991] results for surface and geoid displacements (see Figures 8 and 9, "cos" components, in the work by Wang, in comparison with our semidiurnal maps in Figure 5). For gravity, our results show that tidal gravity perturbations are particularly affected by mantle heterogeneities smaller than those taken into account in Wang's work. For this reason, our results for gravity cannot be significantly compared with Wang's results, however the order of magnitude of the gravity anomalies are globally similar in both studies.

4.2. Time Evolution of Tidal Observations

[22] Although Figure 4 presents tidal perturbations for a single instant in time, tidal signals evolve with time following the gravitation of the Moon and the Sun. We used the tide-generating catalogue developed by *Hartmann and Wenzel* [1995] to theoretically construct the tidal response of the Earth for various locations around the globe during 20 days in November 2007. The amplitudes of gravity magnitude variations (Figure 6, right) are between 1‰ and 0.1‰ of the total magnitudes (Figure 6, left; see Table 1). The larger amplitudes occur near regions of subduction, with semidiurnal tides in Borneo producing maximum perturbations near 100 nGal (Figure 6a) and diurnal tides in Santiago almost as large (Figure 6b). Upper mantle low-velocity structures beneath Djibouti, in eastern Africa, yield perturbations to both diurnal and semidiurnal signals to produce amplitudes close to 100 nGal (Figure 6c). Honolulu (Figure 6d) presents a slightly smaller signal, although close to the 100 nGal limit. Nice (Figure 6e) presents gravity perturbations smaller than 50 nGal, but this level is close to the largest perturbation in Europe. The majority of the world, as well as most of North America, presents an even smaller signal that is exemplified by the signal predicted for Baltimore (Figure 6f).

[23] It should be noted that these gravity signals could even be larger at different times of the year. Although a diurnal component, which exhibits largest amplitudes near the winter solstice, dominates for most places presented here, Borneo presents almost exclusively a semidiurnal pattern. In this case, the maximum is known to be at the equinox. Consequently, the Borneo signal will be even larger in March, with a maximum around 150 nGal.

[24] The patterns of tidal perturbations for displacement (Figure 7) are completely different than those for gravity (Figure 6). Displacement perturbations in Borneo are very small, whereas amplitudes are larger for Santiago, Djibouti, and even Baltimore. This is due to the fact that the displacement perturbations do not present the same geographical patterns as the gravity perturbations, as can be seen in Figures 4 (middle) and 4 (right): displacement and geoid perturbations exhibit very long wavelengths, whereas gravity perturbations present shorter wavelengths, as it is typically the case for gravimetry. While the geoid and elastic deformation fields are typically more sensitive to large lower mantle heterogeneities, gravity is more sensitive to shallower and consequently smaller upper mantle heterogeneities. Figures 6 (right) and 7 (right) are consequently not proportional as they would be for the PREM model. Note also that our calculation is purely elastic. This means that the frequency components of the PREM tidal model are in phase with the associated perturbations. However, the combination of all the frequency components may lead to apparent dephasing in Figures 6 and 7.

4.3. Relative Contributions of the Upper and Lower Mantles

[25] We tested different models of Earth's interior heterogeneity in order to better constrain the source of the mantle heterogeneity that perturbs the solid Earth tides. In partic-

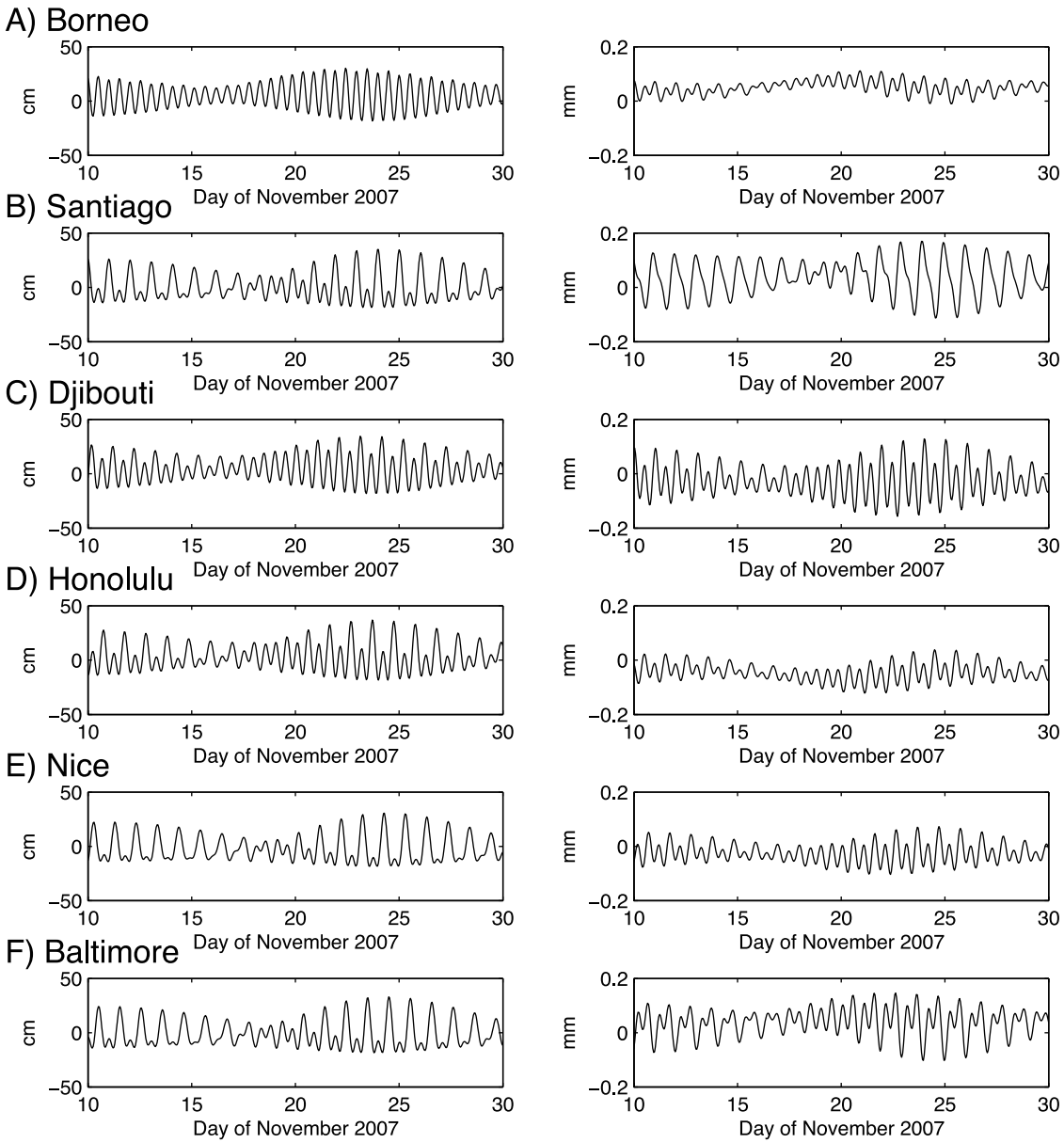

Figure 7. Prediction of radial surface displacement at the same locations as in Figure 6. (left) Graphs of the tidal signal calculated for the PREM Earth model. (right) Graphs of additional perturbations due to mantle lateral heterogeneities and to surface and CMB topographies.

ular, we tested Earth models that restrict mantle lateral heterogeneity to either the upper or lower mantles. Dynamic topographies have been calculated for both models (Figure 2), and the resulting tidal responses were computed as above. We present results (Figure 8) for semidiurnal gravity tides in the same configuration as we did for the whole mantle perturbation (Figure 5c). We found (not shown) that surface and geoid tidal displacements are primarily affected by heterogeneities in the lower mantle. By contrast, perturbations to surface gravity are affected by both upper mantle (Figure 8a) and lower mantle (Figure 8b) structures, with the contribution from the upper mantle being slightly smaller. This observation is consistent with the fact that gravity is more sensitive to shallower structure than is the geoid. However, the relative contributions of the upper and lower mantles on tidal gravity depends on location. In South America and in eastern Asia, tidal gravity anomalies are due to both the lower and upper mantles. However, in eastern Africa the total anomaly primarily reflects the upper mantle contribution. In the Pacific, the contributions from lower mantle superplumes are more important than they are in Africa.

4.4. Relative Contributions of Dynamic Topography and Density Heterogeneity

[26] We also tested the importance of dynamic topography on the CMB and on Earth's surface for body tide perturbations. Without taking into account dynamic topography (and assuming an Earth geoid as in Figure 3a), we find that perturbations to the surface tidal displacement and to the geoid tidal displacement (not shown) present spatial

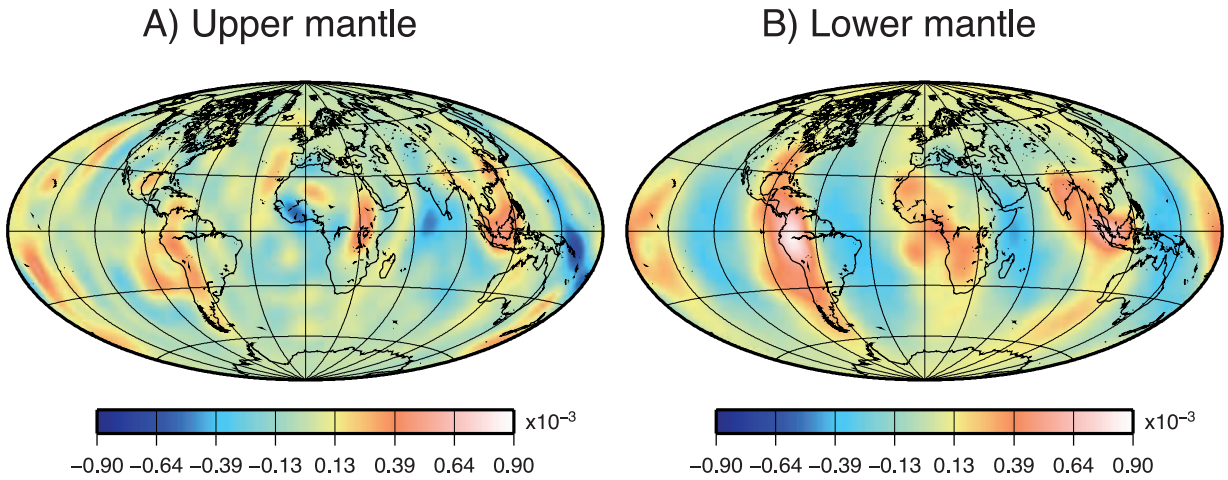

Figure 8. Semidiurnal components of the tidal gravity perturbations (Δ_{2m} with $m = -2$) induced only by the laterally heterogeneous structure in the Earth's (a) upper mantle or its (b) lower mantle. The sum of these two fields is equal to the total tidal gravity perturbations shown in Figure 5a. See Figure 2 for the dynamic topography corresponding to each of these two cases.

patterns that are very similar to the patterns predicted when dynamic topography is included (Figures 4a and 4b), but their magnitudes are about 50% smaller.

[27] For tidal gravity, the picture is more complicated. Without dynamic topography, gravity perturbations calculated in the absence of dynamic topography (Figure 9a) are of approximately the same magnitude as gravity perturbations that we found earlier for an Earth with dynamic topography (Figure 5a). However, this similarity in magnitudes involves a coincidence of two competing effects. First, dynamically supported deformations to the surface and the CMB introduce additional perturbations to the tidal gravity signal. These perturbations tend to reduce the magnitude of the tidal gravity perturbations measured on the tidally perturbed spherical surface by about 40% (Figure 9b). (Note that the surfaces on which Figures 9a and 9b are measured are nearly identical and differ only by the doubling of the tidal displacement that we found to be associated with the introduction of dynamic topography.) However, when the tidal gravity is measured on the surface that has been deformed by the dynamic topography (i.e., the new surface of the Earth), then we find that the amplitude increases back to the level we found for tidal gravity perturbations produced in the absence of dynamic topography. Thus, the two effects approximately cancel, and we find that the net magnitudes of tidal gravity perturbations are similar both with and without dynamic topography (Figures 5a and 9a). The two fields even exhibit similar spatial patterns, although the difference between them (Figure 9c) displays amplitudes that are about half those of either field, which shows that the two fields are not identical. These differences emphasize the importance of dynamic topography to the full calculation of the tidal gravity perturbation field.

4.5. Effect of Rigidity Variations

[28] Finally, we tested the impact of lateral variations of rigidity on our results by removing the lateral variations in rigidity (but not density) everywhere. We found that the contribution of rigidity heterogeneity is small compared to that of density heterogeneity. The impact of rigidity heterogeneity on our results is about 8% for tidal gravity perturbations, and between 15 and 20% for surface and geoid tidal displacement perturbations.

5. Discussion and Conclusions

[29] We have shown that lateral heterogeneities in the mantle's internal structure induce perturbations to the tidal response of a radially symmetric solid Earth of up to almost 1‰ at the Earth's surface. For radial tidal displacements of the Earth's surface or geoid, the maximum expected perturbations are about 0.3 mm and 0.1 mm, respectively. For tidal gravity, the maximum expected perturbation is about 150 nGal. The global pattern of these tidal perturbations is variable: while surface and geoid radial displacements produce long-wavelength perturbations, gravity perturbation anomalies are more localized. As expected by *Métivier et al.* [2007], the surface displacement and geoid perturbations are mostly caused by heterogeneity in the lower mantle, while the gravity perturbations are more sensitive to upper mantle heterogeneity. The deeper source of the displacement-producing heterogeneities induces a long-wavelength structure to these perturbations compared to the gravity perturbations that are more sensitive to shallower upper mantle structure.

[30] Considering the precision of present measurement techniques, the magnitude of surface and geoid displacement perturbations are very small. Though a precision of less than 1 mm can be achieved with GPS measurements [*Petrov and Boy*, 2004], 0.3 mm is below the detection limit. A perturbation of 0.1 mm in geoid displacement corresponds exactly to the precision initially expected from GRACE mission geoid determination [*Dickey et al.*, 1997], but after 5 years, this mission goal has not been achieved [*Tapley et al.*, 2004; *Wahr et al.*, 2006; *Schrama and Visser*, 2007]. Nevertheless, because our predictions of radial displacement perturbations are at the precision limit of present spatial gravimetry, it may be important to take these perturbations into account for body tide models in

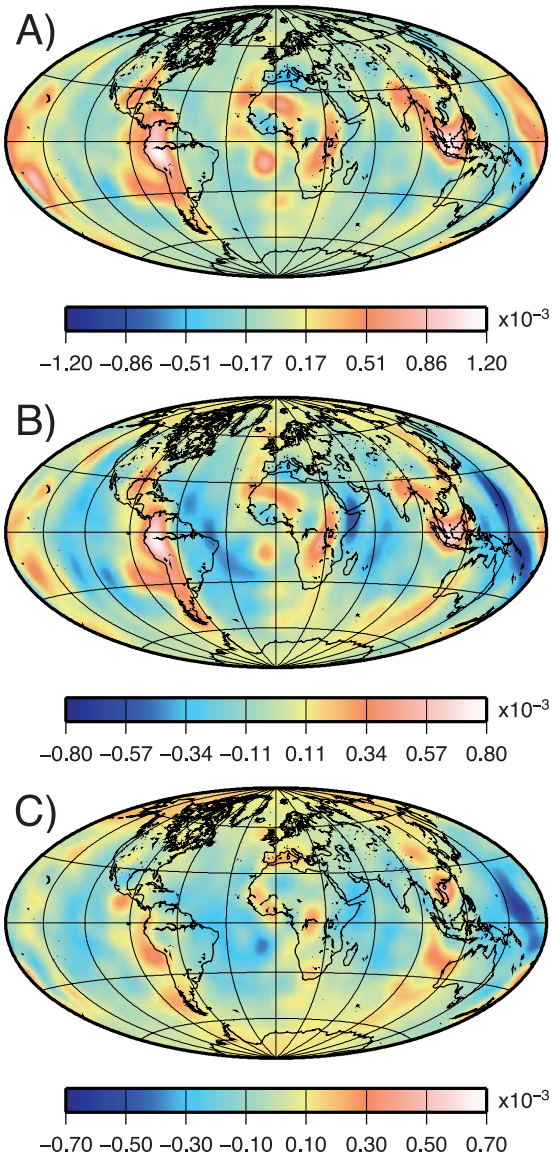

Figure 9. Semidiurnal components of the tidal gravity perturbations (Δ_{2m} with $m = -2$) induced by the laterally heterogeneous structure of the Earth (a) without the presence of dynamic topography on the surface or the CMB and (b) including the dynamic topography on the surface and CMB but measured on the spherical surface that has not been deformed by dynamic topography (but is still subject to tidal deformation). These calculations can be compared to Figure 5a, which shows the total tidal gravity perturbations including both internal density heterogeneity and dynamic topography, measured on a surface that has been deformed by the dynamic topography. (c) The difference between Figure 9a and Figure 5a, thus displaying the changes to the tidal gravity perturbations that are induced by the presence of dynamic topography.

future spatial gravimetry missions (GOCE mission, GRACE Follow On mission). On the other hand, tidal gravity perturbations on the deformed Earth surface present a signal that is one hundred times greater than the precision of superconducting gravimeters. These cryogenic gravimeters are today used in global observatory networks like the Global Geodynamic Project network (GGP) [*Aldridge et al.*, 1991; *Hinderer and Crossley*, 2004] and are known to present an accuracy about 1 nGal (notably in the tidal frequency band after time integration). However, it is well known that the signal measured by gravimeters in the field is dominated by a poorly understood "noise" that is largely greater than the gravimeter precision. This residue, which seems to be up to 300 nGal, is usually thought to be associated with an unmodeled component of oceanic tidal loading [*Agnew*, 1995; *Boy et al.*, 2003; *Baker and Bos*, 2003; *Bos and Baker*, 2005]. Here we have shown that internal heterogeneity caused by thermal convection within the mantle can also introduce "noise" with magnitudes greater than 100 nGal. Thus, the effect of the Earth's internal heterogeneity on body tides may be as important as oceanic tidal loading for perturbing the tidal gravity signal. Furthermore, it may be more feasible to model these body tide perturbations, as we have already achieved here.

[31] *Rosat et al.* [2004] [see also *Ducarme et al.*, 2004; *Xu et al.*, 2004], studied the residue in gravity measurements coming from 19 GGP stations. Unfortunately, most of the stations are located in regions where body tide anomalies are not very large (such as in Europe). However, *Rosat et al.* [2004] noted that the observed residue at the station in Bandung (Indonesia) was larger than that of the other stations. They attributed this observation to complex loading effects due to oceanic tides or to calibration issues. Here we have shown that this region also presents large body tide perturbations induced by mantle dynamics. These body tide perturbations could also explain the observed excess residue for gravity measurement made in Bandung. Because a comparable contribution from oceanic tides remains highly probable in this region, the combination of both effects might explain the very high value of the observed residue.

[32] Body tide perturbations to gravity are not evenly distributed. We can see two major spots (Figures 4c, 6a, 6b, and 6c), above the west coast of South America and above Indonesia-Marianas trench area, where gravity perturbations are greatest. These areas are both near subduction zones, and thus near high-density slabs in the upper mantle. Large amplitude anomalies in the central Pacific and Africa are probably associated with the two famous superplumes. In Africa, the anomaly above the East African Rift is particularly large, which is mostly induced by upwelling heterogeneity in the upper mantle. Finally, smaller spots can be seen above major hot spots like Hawaii and Iceland, or near smaller subduction zones such as those in southern Europe (close to Italy). Our results are quite different from those presented by *Fu and Sun* [2007], particularly with respect to gravity perturbations. In our results, we can clearly observe the signature of known geodynamic and tectonic processes in the body tide perturbations. By contrast, the distribution of perturbations presented by *Fu and Sun* [2007] is more complex. One major difference between our study and that of *Fu and Sun* [2007] is that our study includes the dynamic topography associated with mantle flow, while *Fu and Sun* [2007] only consider the internal heterogeneity within a static (nonconvecting) Earth. As shown above and by many others previously [e.g., *Hager*, 1984; *Richards and Hager*, 1984; *Thoraval and Richards*, 1997; *Čadek and Fleitout*,

2003], both the Earth's internal heterogeneity and the dynamic topography associated with this heterogeneity in a viscous mantle must be included to explain the geoid. As we have shown, both contributions will perturb Earth's body tides.

[33] In conclusion, we have shown that spherical (or elliptical) body tide models are today not sufficient to fully correct all of the observed gravity data. These models should be improved by taking into account the heterogeneous internal structure of the Earth and its asphericity (at wavelengths shorter than the ellipticity). Here we provide all of the information needed to use our results with this aim (Tables S1–S3 in the auxiliary material). It is possible that, with improved modeling and increased accuracy of measurement techniques, body tide perturbations could become a new tool for investigating the mantle's interior structure and dynamics.

[34] **Acknowledgments.** We thank two anonymous reviewers for their helpful comments on the manuscript. The project was supported by the Morton K. and Jane Blaustein Foundation (L.M.) and by NSF grant EAR-0609590 (C.P.C.).

References

Agnew, D. C. (1995), Ocean-load tides at the South Pole: A validation of recent ocean-tide models, *Geophys. Res. Lett.*, *22*(22), 3063–3066.

Aldridge, K., D. J. Crossley, L. Mansinha, and D. Smylie (1991), GGP The Global Geodynamics Project, in *Non Tidal Gravity Changes Intercomparison Between Absolute and Superconducting Gravimeters, Cah. 3*, edited by C. Poitevin, pp. 169–196, Cent. Eur. de Géodyn. et de Séismol., Luxembourg.

Baker, T. F., and M. S. Bos (2003), Validating Earth and ocean tide models using tidal gravity measurements, *Geophys. J. Int.*, *152*(2), 468–485, doi:10.1046/j.1365-246X.2003.01863.x.

Becker, T., and L. Boschi (2002), A comparison of tomographic and geodynamic mantle models, *Geochem. Geophys. Geosyst.*, *3*(1), 1003, doi:10.1029/2001GC000168.

Behn, M. D., C. P. Conrad, and P. G. Silver (2004), Detection of upper mantle flow associated with the African Superplume, *Earth Planet. Sci. Lett.*, *224*, 259–274, doi:10.1016/j.epsl.2004.05.026.

Bos, M. S., and T. F. Baker (2005), An estimate of the errors in gravity ocean tide loading computations, *J. Geod.*, *79*(1–3), 50–63.

Boy, J.-P., M. Llubes, J. Hinderer, and N. Florsch (2003), A comparison of tidal ocean loading models using superconducting gravimeter data, *J. Geophys. Res.*, *108*(B4), 2193, doi:10.1029/2002JB002050.

Čadek, O., and L. Fleitout (2003), Effect of lateral viscosity variations in the top 300 km on the geoid and dynamic topography, *Geophys. J. Int.*, *152*, 566–580, doi:10.1046/j.1365-246X.2003.01859.x.

Chaljub, E., Y. Capdeville, and J.-P. Vilotte (2003), Solving elastodynamics in a fluid-solid heterogeneous sphere: A parallel spectral element approximation on non-conforming grids, *J. Comput. Phys.*, *187*, 457–491.

Colin, P., and L. Fleitout (1990), Topography of the ocean floor: Thermal evolution of the lithosphere and interaction of deep mantle heterogeneities with the lithosphere, *Geophys. Res. Lett.*, *17*, 1961–1964.

Conrad, C. P., and M. Gurnis (2003), Seismic tomography, surface uplift, and the breakup of Gondwanaland: Integrating mantle convection backwards in time, *Geochem. Geophys. Geosyst.*, *4*(3), 1031, doi:10.1029/2001GC000299.

Conrad, C. P., C. Lithgow-Bertelloni, and K. E. Louden (2004), Iceland, the Farallon slab, and dynamic topography of the North Atlantic, *Geology*, *32*, 177–180, doi:10.1130/G20137.1.

Conrad, C. P., M. D. Behn, and P. G. Silver (2007), Global mantle flow and the development of seismic anisotropy: Differences between the oceanic and continental upper mantle, *J. Geophys. Res.*, *112*, B07317, doi:10.1029/2006JB004608.

Courtillot, V., A. Davaille, J. Besse, and J. Stock (2003), Three distinct types of hotspots in Earth's mantle, *Earth Planet. Sci. Lett.*, *205*, 295–308.

Crossley, D., J. Hinderer, and M. Amalvict (2001), A spectral comparison of absolute and superconducting gravimeter data, *J. Geod. Soc. Jpn.*, *47*, 373–376.

Dahlen, F. A., and J. Tromp (1998), *Theoretical Global Seismology*, Princeton Univ. Press, Princeton, N. J.

Davaille, A. (1999), Simultaneous generation of hotspots and superswells by convection in a heterogeneous planetary mantle, *Nature*, *402*, 756–760.

Dehant, V. (1987), Tidal parameters for an inelastic Earth, *Phys. Earth Planet. Inter.*, *49*, 97–116.

Dehant, V., P. Defraigne, and J. M. Wahr (1999), Tides for a convective Earth, *J. Geophys. Res.*, *104*, 1035–1058.

Dickey, J. O., et al. (1997), *Satellite Gravity and the Geosphere*, Natl. Res. Counc., Natl. Acad. Press, Washington, D. C.

Ducarme, B., A. P. Venedikov, J. Arnoso, and R. Vieira (2004), Determination of the long period tidal waves in the GGP superconducting gravity data, *J. Geodyn.*, *38*, 307–324.

Dziewonski, A. M., and D. L. Anderson (1981), Preliminary reference Earth model, *Phys. Earth Planet. Inter.*, *25*, 297–356.

Fu, G., and W. Sun (2007), Effects of lateral inhomogeneity in a spherical Earth on gravity Earth tides, *J. Geophys. Res.*, *112*, B06409, doi:10.1029/2006JB004512.

Grand, S. P., R. D. van der Hilst, and S. Widiyantoro (1997), Global seismic tomography: A snapshot of convection in the Earth, *GSA Today*, *7*, 1–7.

Greff-Lefftz, M., L. Métivier, and H. Legros (2005), Analytical solutions of Love numbers for an hydrostatic ellipsoidal incompressible homogeneous Earth, using Lagrangian formulation, *Celest. Mech. Dyn. Astron.*, *93*, 113–146.

Gu, Y. J., A. M. Dziewonski, W. J. Su, and G. Ekström (2001), Models of the mantle shear velocity and discontinuities in the pattern of lateral heterogeneities, *J. Geophys. Res.*, *106*, 11,169–11,199.

Gurnis, M. (1993), Phanerozoic marine inundation of continents driven by dynamic topography above subducting slabs, *Nature*, *364*, 589–593, doi:10.1038/364589a0.

Hager, B. H. (1984), Subducted slabs and the geoid: Constraints on mantle rheology and flow, *J. Geophys. Res.*, *89*, 6003–6015.

Hartmann, T., and H. G. Wenzel (1995), The HW95 tidal potential catalogue, *Geophys. Res. Lett.*, *22*(24), 3553–3556.

Hinderer, J., and D. Crossley (2004), Scientific achievements from the first phase (1997–2003) of the global geodynamics project using a worldwide network of superconducting gravimeters, *J. Geodyn.*, *38*(3–5), 237–262.

Husson, L. (2006), Dynamic topography above retreating subduction zones, *Geology*, *34*, 741–744, doi:10.1130/2FG22436.1.

Jordan, T. H. (1975), The continental tectosphere, *U.S. Natl. Rep. Int. Union Geod. Geophys. 1971–1974, Rev. Geophys. Space Phys.*, *13*(3), 1–12.

Karato, S., and B. B. Karki (2001), Origin of lateral variation of seismic wave velocities and density in the deep mantle, *J. Geophys. Res.*, *106*(B10), 21,771–21,783, doi:10.1029/2001JB000214.

Komatitsch, D., and J. Tromp (1999), Introduction to the spectral element method for three-dimensional seismic wave propagation, *Geophys. J. Int.*, *139*, 806–822.

Li, X.-D., and B. Romanowicz (1996), Global mantle shear velocity model developed using nonlinear asymptotic coupling theory, *J. Geophys. Res.*, *101*, 22,245–22,272, doi:10.1029/96JB01306.

Lithgow-Bertelloni, C., and M. A. Richards (1998), The dynamics of Cenozoic and Mesozoic plate motions, *Rev. Geophys.*, *36*, 27–78.

Lithgow-Bertelloni, C., and P. G. Silver (1998), Dynamic topography, plate driving forces and the African superswell, *Nature*, *395*, 269–272, doi:10.1038/26212.

Love, A. E. H. (1911), *Some Problems of Geodynamics*, Dover, New York.

Masters, G., G. Laske, H. Bolton, and A. M. Dziewonski (2000), The relative behavior of shear velocity, bulk sound speed, and compressional shear velocity in the mantle: Implications for chemical and thermal structure, in *Earth's Deep Interior: Mineral Physics and Tomography from the Atomic to the Global Scale*, *Geophys. Monogr. Ser.*, vol. 117, edited by S.-I. Karaoa et al., pp. 709–728, AGU, Washington, D. C.

Mathews, P. M., B. A. Buffet, and I. I. Shapiro (1995), Love numbers for a rotating spheroidal Earth: New definitions and numerical values, *Geophys. Res. Lett.*, *22*, 579–582.

Melchior, P. (1995), A continuing discussion about the correlation of tidal gravity anomalies and heat flow densities, *Phys. Earth Planet. Inter.*, *88*, 223–256.

Métivier, L., M. Greff-Lefftz, and M. Diament (2005), A new approach to compute accurate gravity time variations for a realistic Earth model with lateral heterogeneities, *Geophys. J. Int.*, *162*, 570–574.

Métivier, L., M. Greff-Lefftz, and M. Diament (2006), Mantle lateral variations and elasto-gravitational deformations - I. Numerical modeling, *Geophys. J. Int.*, *167*, 1060–1076, doi:10.1111/j.1365-246X.2006.03159.x.

Métivier, L., M. Greff-Lefftz, and M. Diament (2007), Mantle lateral variations and elasto-gravitational deformations - II. Possible effects of a superplume on body tides, *Geophys. J. Int.*, *168*, 897–903, doi:10.1111/j.1365-246X.2006.03309.x.

Mitrovica, J. X., C. Beaumont, and G. T. Jarvis (1989), Tilting of continental interiors by the dynamical effects of subduction, *Tectonics*, *8*, 1079–1094.

Molodenskiy, S. M. (1977), The influence of horizontal inhomogeneities in the mantle on the amplitude of the tidal oscillations, *Izv. Earth Phys.*, *13*, 77–80.

Montelli, R., G. Nolet, F. A. Dahlen, and G. Masters (2006), A catalogue of deep mantle plumes: New results from finite-frequency tomography, *Geochem. Geophys. Geosyst.*, *7*, Q11007, doi:10.1029/2006GC001248.

Moresi, L., S. Zhong, and M. Gurnis (1996), The accuracy of finite element solutions of Stokes' flow with strongly varying viscosity, *Phys. Earth Planet. Inter.*, *97*, 83–94.

Petrov, L., and J.-P. Boy (2004), Study of the atmospheric pressure loading signal in very long baseline interferometry observations, *J. Geophys. Res.*, *109*, B03405, doi:10.1029/2003JB002500.

Pysklywec, R. N., and J. X. Mitrovica (1998), Mantle flow mechanisms for the large-scale subsidence of continental interiors, *Geology*, *26*, 687–690.

Reigber, C., R. Schmidt, F. Flechtner, R. Konig, U. Meyer, K. H. Neumayer, P. Schwintzer, and S. Y. Zhu (2005), An Earth gravity field model complete to degree and order 150 from GRACE: EIGEN-GRACE02S, *J. Geodyn.*, *39*, 1–10.

Richards, M. A., and B. H. Hager (1984), Geoid anomalies in a dynamic Earth, *J. Geophys. Res.*, *89*, 5987–6002.

Ritsema, J., H. J. van Heijst, and J. H. Woodhouse (1999), Complex shear wave velocity structure imaged beneath Africa and Iceland, *Science*, *286*, 1925–1928, doi:10.1126/science.286.5446.1925.

Ritsema, J., H. J. van Heijst, and J. H. Woodhouse (2004), Global transition zone tomography, *J. Geophys. Res.*, *109*, B02302, doi:10.1029/2003JB002610.

Robinson, E. S. (1989), Tidal gravity, heat flow, and the upper crust, *Phys. Earth Planet. Inter.*, *56*, 181–185.

Romanowicz, B., and Y. Gung (2002), Superplumes from the core-mantle boundary to the lithosphere: Implications for heat flux, *Science*, *296*, 513–516, doi:10.1126/science.1069404.

Rosat, S., J. Hinderer, D. Crossley, and J. P. Boy (2004), Performance of superconducting gravimeters from long-period seismology to tides, *J. Geodyn.*, *38*(3–5), 461–476.

Rydelek, P. A., W. Zürn, and J. Hinderer (1991), On tidal gravity, heat flow and lateral heterogeneities, *Phys. Earth Planet. Inter.*, *91*, 215–229.

Schrama, E. J. O., and P. N. A. M. Visser (2007), Accuracy assessment of the monthly GRACE geoids based upon a simulation, *J. Geod.*, *81*, 67–80, doi:10.1007/s00190-006-0085-1.

Smith, M. L. (1974), The scalar equations of infinitesimal elastic-gravitational motion for a rotating, slightly elliptical Earth, *Geophys. J. R. Astron. Soc.*, *37*, 491–526.

Tapley, B. D., S. Bettadpur, M. Watkins, and C. Reigber (2004), The gravity recovery and climate experiment: Mission overview and early results, *Geophys. Res. Lett.*, *31*, L09607, doi:10.1029/2004GL019920.

Tapley, B., et al. (2005), GGM02—An improved Earth gravity field model from GRACE, *J. Geod.*, *79*, 467–478, doi:10.1007/s00190-005-0480-z.

Thoraval, C., and M. A. Richards (1997), The geoid constraint in global geodynamics: Viscosity structure, mantle heterogeneity models and boundary conditions, *Geophys. J. Int.*, *131*(1), 1–8, doi:10.1111/j.1365-246X.1997.tb00591.x.

Van Camp, M., S. D. P. Williams, and O. Francis (2005), Uncertainty of absolute gravity measurements, *J. Geophys. Res.*, *110*, B05406, doi:10.1029/2004JB003497.

van der Hilst, R., S. Widiyantoro, and E. Engdahl (1997), Evidence for deep mantle circulation from global tomography, *Nature*, *386*, 578–584.

Wahr, J., S. Swenson, and I. Velicogna (2006), Accuracy of GRACE mass estimates, *Geophys. Res. Lett.*, *33*, L06401, doi:10.1029/2005GL025305.

Wahr, J. M. (1981a), A normal mode expansion for the forced response of a rotating Earth, *Geophys. J. R. Astron. Soc.*, *64*, 651–675.

Wahr, J. M. (1981b), Body tides on an elliptical, rotating, elastic and oceanless Earth, *Geophys. J. R. Astron. Soc*, *64*, 677–703.

Wahr, J. M., and Z. Bergen (1986), The effects of mantle anelasticity on nutations, Earth tides, and tidal variations in rotation rate, *Geophys. J. R. Astron. Soc.*, *64*, 633–668.

Wang, R. (1991), Tidal deformations of a rotating, spherically asymmetric, visco-elastic and laterally heterogeneous Earth, Ph.D. thesis, Univ. of Kiel, Kiel, Germany.

Woodhouse, J. H., and F. A. Dahlen (1978), The effect of a general aspherical perturbation on the free oscillations of the Earth, *Geophys. J. R. Astron. Soc.*, *53*, 335–354.

Xu, J., H. Sun, and B. Ducarme (2004), A global experimental model for gravity tides of the Earth, *J. Geod.*, *38*, 293–306, doi:10.1016/j.jog.2004.07.003.

Zhong, S., M. T. Zuber, L. Moresi, and M. Gurnis (2000), Role of temperature-dependent viscosity and surface plates in spherical shell models of mantle convection, *J. Geophys. Res.*, *105*, 11,063–11,082, doi:10.1029/2000JB900003.

C. P. Conrad, Department of Geology and Geophysics, University of Hawaii, 1680 East-West Road, Honolulu, HI 96822, USA.

L. Métivier, Department of Earth and Planetary Sciences, Johns Hopkins University, Olin Hall, 3400 North Charles Street, Baltimore, MD 21218, USA. (metivier@jhu.edu)